Journal of the Optical Society of Korea
Vol. 14, No. 4, December 2010, pp. 431-437
DOI: 10.3807/JOSK.2010.14.4.431

# The Optical Design of Probe-type Microscope Objective for Intravital Laser Scanning CARS Microendoscopy

**Cheon-Seog Rim***

*Department of Physics, Hannam University, 133 Daedeok-gu, Daejeon 306-791, Korea*

(Received October 5, 2010 : revised November 12, 2010 : accepted November 15, 2010)

A stack of gradient-index (GRIN) rod lenses cannot be used for coherent anti-Stokes Raman scattering (CARS) microendoscopy for insertion to internal organs through a surgical keyhole with minimal invasiveness. That's because GRIN lens has large amount of inherent chromatic aberrations in spite of absolutely requiring a common focus for pump and Stokes beam with each frequency of $\omega_p$ and $\omega_S$. For this endoscopic purpose, we need to develop a long slender probe-type objective, namely probe-type microscope objective (PMO). In this paper, we introduce the structure, the working principle, and the design techniques of PMO which is composed of a probe-type lens module (PLM) and an adaptor lens module (ALM). PLM is first designed for a long slender type and ALM is successively designed by using several design parameters from PLM for eliminating optical discords between scanning unit and PLM. A combined module is optimized again to eliminate some coupling disparities between PLM and ALM for the best PMO. As a result, we can obtain a long slender PMO with perfectly diffraction-limited performance for pump beam of 817 nm and Stokes beam of 1064 nm.

*Keywords* : Microscope probe objective, Microendoscopy, Coherent anti-Stokes Raman scattering, CARS microscopy, Two photon fluorescence microscopy
*OCIS codes* : (220.0220) Optical design and fabrication; (110.0180) Microscopy; (220.3620) Lens system design; (300.6230) Spectroscopy, coherent anti-Stokes Raman scattering

## I. INTRODUCTION

Obtaining molecular imaging in living organisms is applicable to the diagnosis of diseases such as cancer and cardiovascular disease [1-3]. This imaging technique can also be utilized in treating these kinds of disorders by testing the clinical effects of new medication. Non linear optical (NLO) microscopy is a candidate being actively researched in this field. It can obtain the resolution of several hundreds of nanometers. So to speak, NLO microscopy is actively utilized to image the cellular details of many organs and disease processes including cell trafficking, cell migration, and molecular interactions [4-8]. The terminology of NLO microscopy actually includes all the microscopies based on multi-photon interactions such as two-photon excitation fluorescence (TPEF) microscopy, second harmonic generation (SHG) microscopy, sum frequency generation (SFG) microscopy, and coherent anti-Stokes Raman scattering (CARS) microscopy. Among these kinds of microscopies, coherent anti-Stokes Raman scattering (CARS) microscopy is preferred to other microscopies because of label-free strong vibrational signals, namely no use of fluorescent dyes [9-11]. However, in spite of this merit of CARS microscopy, multimodality based on CARS microscopy is preferable to CARS only [12-13], because different NLO microscopies each have their distinct advantages in visualizing morphological details.

When we are going to construct CARS microscopy, the microscope is absolutely required to be inserted into a living body. We know well that conventional microscope objective is so bulky that it cannot be inserted into a living body. To achieve this purpose with minimal invasiveness, we need a long slender probe-type objective, namely a probe-type microscope objective (PMO). That is, a PMO which can be inserted to internal organs through a surgical keyhole.

As a candidate for PMO, a stack of cylindrical gradient-index (GRIN) rod lenses can be easily imagined and

*Corresponding author: csrim@hnu.kr
Color versions of one or more of the figures in this paper are available online.

considered. Researchers often utilize GRIN rod lenses for microscope probes [14-20]. There are mainly two cases : in vivo confocal microendoscopy connected with a fiber bundle and in vivo two-photon (or multi-photon) micro-endoscopy coupled with a conventional microscope objective. However, GRIN rod lenses are difficult to use in CARS microendoscopy unlike confocal or multi-photon micro-endoscopy, because the CARS signal is generated only at a coincidence focal point of the pump and Stokes beam with frequencies of $\omega_p$ and $\omega_S$, respectively [12]. GRIN rod lenses have large amount of inherent chromatic aberration which cannot bring a focus for both frequency of $\omega_p$ and $\omega_S$ [21-22].

Meanwhile, there might be another choice of PMO, which is equipped with up to four lasers (488/561/633/748 nm) by Olympus Inc. for multicolor fluorescence. However, this PMO is also difficult to apply for CARS micro-endoscopy, because CARS microscopy chiefly uses near infrared wavelengths, namely 817 nm for pump beam and 1064 nm for Stokes beam. In addition to this reason, the PMO is not easily accessible from Olympus Inc. because of some patent problems. In order to stand at the leading edge of world class development, it is essential that an optical system development like PMO goes with molecular imaging technology. In this paper, we introduce the design procedures and techniques of PMO, especially for CARS imaging.

## II. DESIGN IDEAS AND DESIGN REQUIRMENTS

Coherent anti-Stokes Raman scattering (CARS) signal arises only at a focal point by two laser pulses with the frequencies of both $\omega_p$ and $\omega_S$, called pump and Stokes beam. This means that the signal efficiency is strongly dependent on chromatic aberration between two frequencies. When the beat frequency of $\omega_p$ - $\omega_S$ is tuned to be resonant with a given molecule vibration ($\omega_v$), a strong anti-Stokes signal is coherently driven at $\omega_{as} = 2\omega_p - \omega_S$ (Fig. 1A) [23]. A major improvement since the first attempt of CARS microscopy by Duncan and co-workers in 1982 [24] was the development of the use of near infrared pump (800 nm) and Stokes beam (1200 nm) by Zumbusch and co-workers [25]. This is because near infrared frequencies instead of visible ones can more effectively reduce scattering and photo damage to the in vivo sample. And it is important to realize that the sensitivity of CARS detection is limited by non-resonant contributions such as the non-resonant CARS signal (Fig. 1B) and two-photon enhanced non-resonant signal (Fig. 1C). The use of near infrared frequencies can avoid the two-photon enhanced non-resonant contribution and lead to a significant improvement in sensitivity. Therefore, the frequencies (or wavelengths) of pump and Stokes beams are determined by the research of Conor L. Evans and co-workers [12] who used 817 nm for pump beam and 1064 nm for Stokes beam for multimodality based on CARS microscopy.

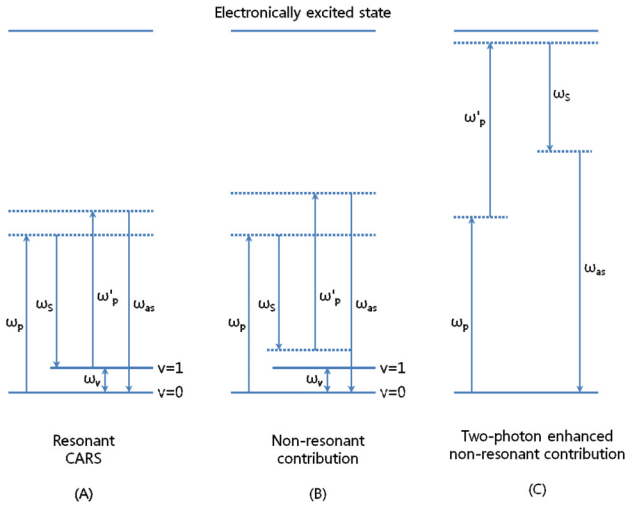


FIG. 1. Resonant and non-resonant contributions for CARS signal. (A) Resonant CARS. (B) Non-resonant CARS due to the third-order susceptibility, where the dotted lines indicate virtual states. (C) Two-photon resonance of pump beam associated with the excited electronic state.

As mentioned above, CARS signal is generated at a coincident focus by the third-order electronic interaction between two pulses and molecular resonant vibration. It is known that resonant CARS signal is proportional to the square of induced third-order polarization, namely $P^{(3)}$ as shown in Eq. (1). Therefore, the signal generation efficiency is proportional to the second order power of pump beam intensity ($I_p^2$) times the first order power of Stokes beam intensity ($I_s$) [23]. This leads to the critical condition for tight focusing without chromatic aberrations, so that PMO has to be perfectly corrected on monochromatic and chromatic aberrations.

$$P^{(3)}(\omega_{as}) \propto \chi^{(3)} E_p(\omega_p) E_s^*(\omega_s) E_p(\omega'_p) \quad (1)$$

where, $\chi^{(3)}$ denotes induced third-order susceptibility for the electronic interaction. $E_p(\omega_p)$ and $E_s(\omega_s)$ denote the electric fields for pump and Stokes beam. And $E_p(\omega'_p)$ denotes the second interaction between pump beam and molecular vibration.

Let's see the schematic working structure of CARS micros-cope. Fig. 2 shows a typical schematic diagram of an intravital laser scanning CARS microscope [26-27]. As shown in Fig. 2, PMO is composed of probe lens module (PLM) and adaptor lens module (ALM), in which PLM can be inserted to an internal organ through a surgical keyhole with minimal invasiveness. And intermediate image plane exists to mutually couple ALM to PLM. When collimated beams are incident on ALM from a scanning unit, ALM is expected to make a focal locus on an intermediate image plane. PLM is also expected to transfer this focal locus to the sample with tight focusing. If the focal points are tightly

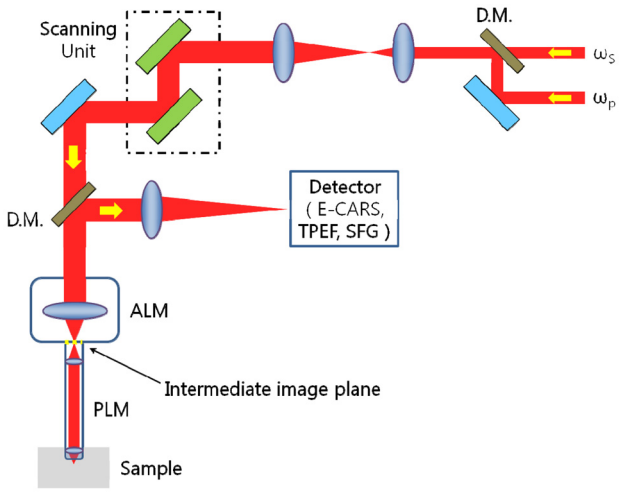


FIG. 2. A typical schematic diagram of an intravital laser scanning CARS microscope with probe-type microscope objective (PMO) which is composed of adaptor lens module (ALM) and probe lens module (PLM), where E-CARS, TPEF, and SFG denote epi-dectected CARS, two-photon excitation fluorescence, and sum frequency generation signal, respectively. D.M., dichroic mirror.

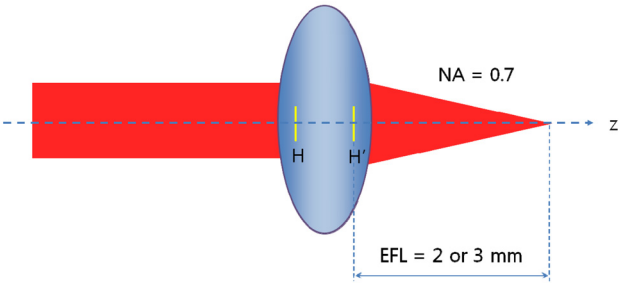


FIG. 3. A short type microscope objective, where H and H' denotes first and second principle point and EFL denotes effective focal length.

made on the sample plane, CARS signal arises at an each point and returned back to the detector after through PLM and ALM by turns. Summarizing the role of PLM and ALM, we can say that PLM and ALM correspond to a stack of GRIN rod lenses and a conventional microscope objective in two-photon fluorescence microscopy, respectively.

We have decided on the structure of probe-type microscope objective (PMO) which consists of PLM and ALM without a detailed explanation. If PMO is expected to consist of only one module as in Fig. 3, there is no way for PMO to be a long slender type. A miniaturized microscope objective might have an effective focal length of about 2 or 3 mm. This causes the diameter of the clear aperture to be at least 2.8 mm for a numerical aperture of 0.7 and short length of probe. In order to be a long slender type, the use of an effective focal length of 20 mm brings the diameter of the clear aperture to be 28 mm. Therefore, PMO has to consist of PLM and ALM and ALM has to make a

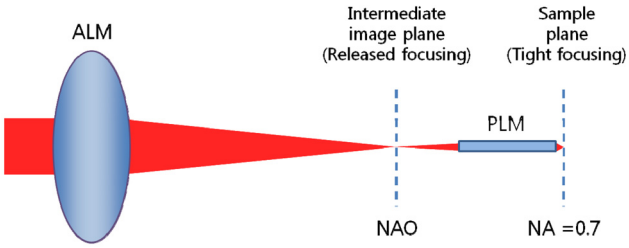


FIG. 4. A long slender type microscope objective which is composed of adaptor lens module (ALM) and probe lens module (PLM), where NAO denotes numerical aperture at object side (or intermediate image side) and NA denotes numerical aperture at image side (or sample side) .

released focusing which causes PLM to be a miniaturized aperture, as shown in Fig. 4. The rest of the design requirements are determined by the Olympus PMO. It has the specifications such as outer diameter of 3.5 mm, field of view of 0.22 mm, numerical aperture of 0.7 at sample side, and length of PLM of 25 mm.

## III. OPTICAL DESIGN OF PROBE LENS MODULE

In order to design a long slender type, we must first consider two key factors: intermediate image height and numerical aperture (NA) on the sample side. Refer Fig. 5, which has already been designed by our design group for a coherent anti-Stokes Raman scattering (CARS) imaging catheter system with fiber bundle. As shown in Fig. 5, almost the whole of the clear aperture is determined by NA. This system requires a 10.4 mm total track length from the fiber bundle end to the sample plane. For a longer total track length, the object plane has to be far away from the first lens surface. This will cause the diameter of clear aperture to be larger than 1.9 mm. Considering the outer diameter of 3.5 mm with the probe length of 25 mm for Olympus PMO (probe-type microscope objective) [19, 26], it can be reasonable to choose the maximum clear aperture of 3.0 mm allowing for steel barrel thickness of 0.25 mm. Then, the total track length of 10.4 mm can be lengthened up to the intermediate image height ($\eta$) of 1.5 mm corresponding to the half of the maximum clear aperture of 3.0 mm. This also leads to NAO of 0.05 by the magnification relationship of PLM. NAO of 0.05 means the released focusing for ALM in Fig. 4, which leads to high structural stability in tolerance level for the whole PMO.

Since the length of PLM has to be 25 mm, an air gap of 15 mm is inserted between the intermediate image plane and the first lens surface in Fig. 5. Fig. 5 is re-optimized to reach a goal of a long slender type without aberrations by CODE V [28]. In optimization, NAO (numerical aperture at object side) is kept to 0.05 and a merit function is composed of the square summation of Seidel 3$^{rd}$ order aber-

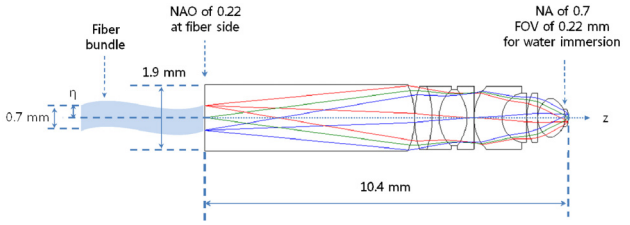


FIG. 5. A miniaturized microscope objective for CARS imaging catheter with fiber bundle which the magnification relationship is given to |M| = NAO/NA = η'/η, where , |M| denotes the absolute value of magnification, η denotes half the diameter of fiber bundle, and η' denotes half field of view (FOV) . Effective focal length of this system is also given to be 2.975 mm.

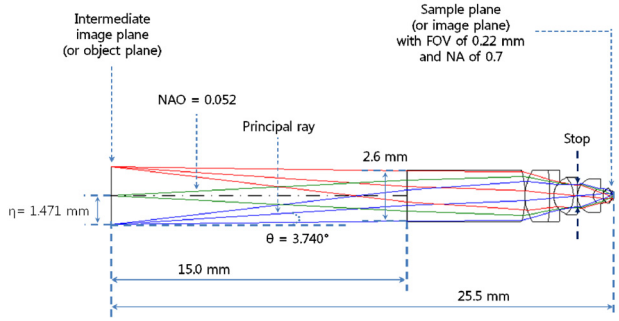


FIG. 6. The final form of PLM with the length of 25.5 mm and the diameter of clear aperture of 2.94 mm, where θ means angle between horizontal dashed line and principal ray. Effective focal length of this system is given to 2.34 mm.

rations, 1st order chromatic aberrations, and general ray aberrations as in our previous research. Fig. 6 shows the final form of PLM with the length of 25.5 mm and the diameter of clear aperture of 2.94 mm. And the final performances of Fig. 6 are shown in Fig. 7, Fig. 8, and Fig. 9. The radius of Airy disk, namely R = 0.61 λ/NA, is given as 0.71 μm for pump beam of 817 nm and 0.93 μm for Stokes beam of 1064 nm. Fig. 7 shows the focus quality in terms of longitudinal spherical aberration (LSA) and astigmatic field curve (AFC). LSA represents focus errors on the sample plane arising from an on-axis point source on the object plane (or intermediate image plane). Refer to Fig. 6. And AFC also represents focus errors on the sample plane arising from an off-axis end point, namely 1.47 mm. As shown in Fig. 7, focus errors are completely corrected for both LSA and AFC. Especially, it is noted that the maximum focus deviations between pump and Stokes beam are 0.06 μm for LSA and 0.29 μm for AFC. Fig. 8 shows spot diagrams for on-axis, 0.7 field, and 1.0 field (off-axis end) on sample plane. As shown in Fig. 8, it is confirmed that there are almost no position deviations between pump and Stokes beam. And since the radius of 100 % of encircled energy is given to be half of 1.67 μm, namely 0.84 μm, it can be said that PLM has

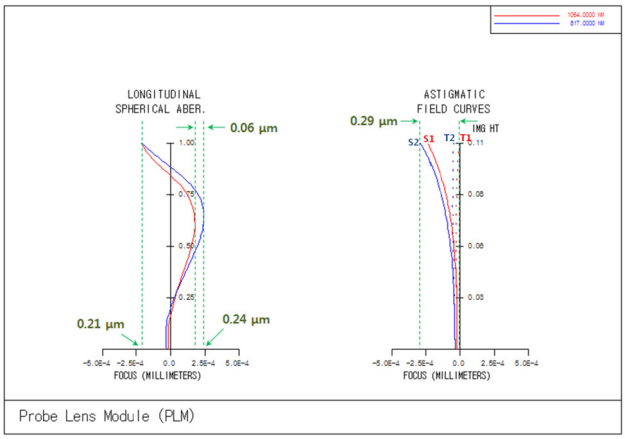


FIG. 7. The focus quality charts which are longitudinal spherical aberration (LSA) and astigmatic field curve (AFC). In charts, 2.5E-4 mm denotes 0.00025 mm or 0.25 μm. T1 or S1 means the curved focus locus of tangential plane (yz) or sagittal plane (xz) for Stokes beam of 1064 nm and T2 or S2 denotes for pump beam of 817 nm.

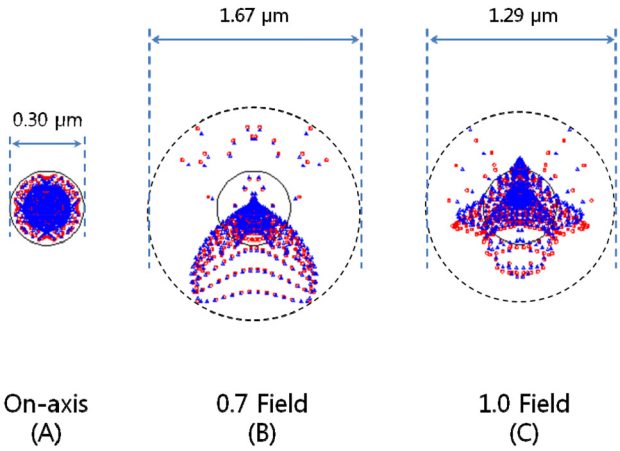


FIG. 8. Spot diagrams. (A) On-axis ( Strehl ratio of 0.999 and RMS wavefront of 0.006 waves for pump beam of 817 nm). (B) 0.7 field (Strehl ratio of 0.989 and RMS wavefront of 0.017 waves for pump beam of 817 nm). (C) 1.0 field (Strehl ratio of 0.983 and RMS wavefront of 0.021 waves for pump beam of 817 nm). Red and blue marks denote Stokes and pump beam, respectively.

nearly diffraction-limited performance without chromatic aberrations considering the criterions of the Airy disk.

## IV. OPTICAL DESIGN OF ADAPTER LENS MODULE

After finishing the design of the probe lens module (PLM) as a long slender type, we have to design the adaptor lens module (ALM) to link between the scanning unit and PLM. As shown in Fig. 2, the two input laser beams with

frequency of $\omega_p$ and $\omega_s$ are synchronously scanned on ALM and then form of focal points on intermediate image plane. Refer to Fig. 4. The intermediate image plane becomes the object plane at the same time for PLM. In the design of ALM, the most difficult problem is to find how to link between the scanning unit and PLM. Let's consider Fig. 9 which shows the geometrical relationship between ALM and PLM. From a fundamental Euclidean geometry of the triangle formed of between optical axis and principal ray [29-31], we can write Eq. (2).

$$s : \eta = (s + f_a) : (s + f_a) \times \tan\theta \quad (2)$$

By a little algebraic calculation, Eq. (2) can be expressed as Eq. (3).

$$f_a = |(s^2\tan\theta - \eta s)/(\eta - s\tan\theta)| = |s| \quad (3)$$

Because alternate angles are equal, s can be expressed as Eq. (4).

$$s = \eta/\tan\theta \quad (4)$$

And the diameter of the aperture stop is given to Eq. (5) from the definition of f-number.

$$D = 2(NAO)f_a \quad (5)$$

If we consider three parameters given from the designed data of PLM such as $\theta$ = 3.740°, $\eta$ = 1.471 mm, and NAO = 0.052, Eq. (3) and Eq. (5) give 22.503 mm as effective focal length ($f_a$) of ALM and Eq. (5) gives 2.356 mm to the diameter of aperture stop (D). An important thing is still left now. We have to decide the location of the aperture stop by from the principal ray. The principal ray passes through the center of the aperture stop and then is refracted by ALM keeping angle ($\theta$) of 3.740° in the direction of the optical axis, as shown in Fig. 9. As a result, we have to keep the following 5 design parameters in the optimization process: $f_a$ of 22.503 mm, D of 2.356 mm, $\theta$ of 3.740°, $\eta$ of 1.471 mm, and NAO of 0.052.

As in the design of PLM, ALM needs initial data for optimization. See Fig. 10 which is extracted from Japanese patents. Fig. 10 is a conventional microscope objective which consists of the front focal length ($f_f$) of 1969.1 mm and the rear focal length ($f_r$) of 46.8 mm. Because the front focal length can be negligible compared to the rear focal length, the front part of the optical system is excluded before optimization. As in the optimization of PLM, we minimize a merit function which is composed of the square summation of Seidel 3rd order aberrations, 1st order chromatic aberrations, and general ray aberrations. As a result of optimization, the final form of ALM and spot diagrams are presented in Fig. 11 and Fig. 12. And the radius of Airy disk, namely R = 0.61 λ/ NA, is given as 9.52 μm for pump beam of 817 nm and 12.40 μm for

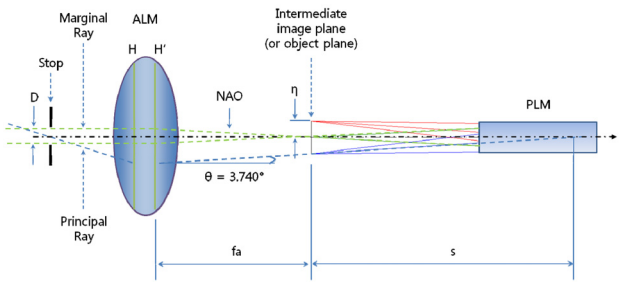


FIG. 9. The geometrical relationship between ALM and PLM.

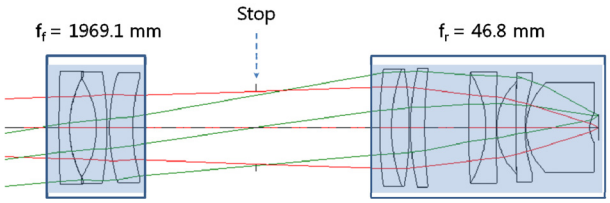


FIG. 10. An initial data for optimization which is extracted from Japan patents.

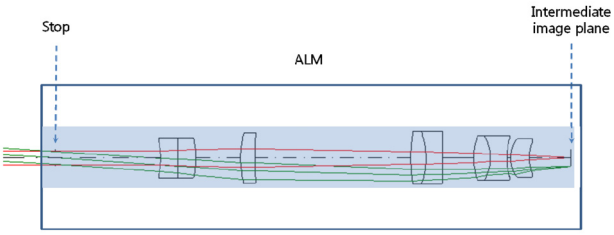


FIG. 11. The final form of ALM with $f_a$ of 22.503 mm, D of 2.356 mm, $\theta$ of 3.740°, $\eta$ of 1.471 mm, and NAO of 0.052.

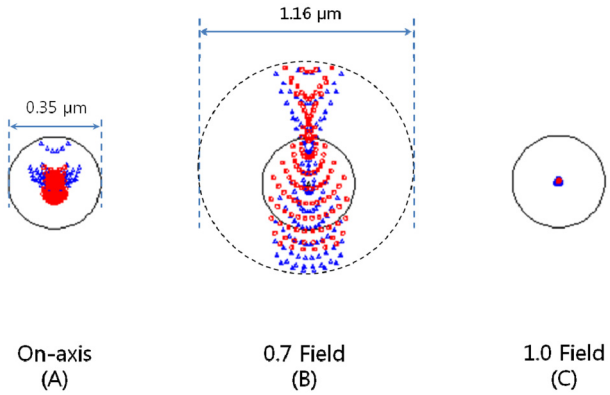


FIG. 12. Spot diagrams. (A) On-axis ( Strehl ratio of 1.000 and RMS wavefront of 0.001 waves for pump beam of 817 nm). (B) 0.7 field (Strehl ratio of 0.999 and RMS wavefront of 0.005 waves for pump beam of 817 nm). (C) 1.0 field (Strehl ratio of 1.000 and RMS wavefront of 0.001 waves for pump beam of 817 nm). Red and blue marks denote Stokes and pump beam, respectively.

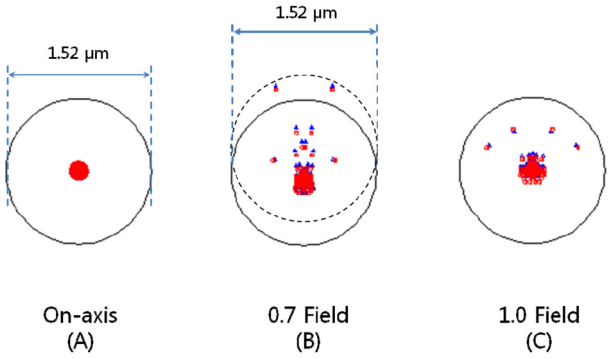


FIG. 13. The final form of probe-type microscope objective (PMO) which consists of ALM and PLM with field of view of 0.22 mm and numerical aperture of 0.7 at sample side.

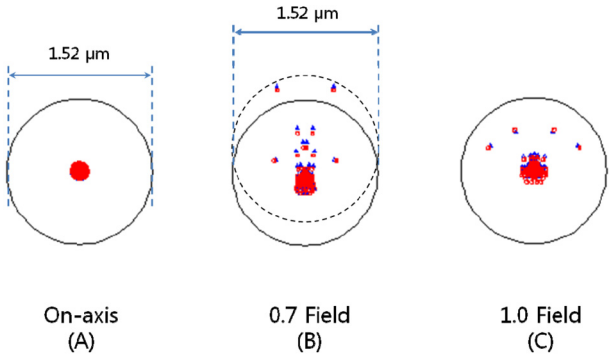


FIG. 14. Spot diagrams. (A) On-axis ( Strehl ratio of 0.999 and RMS wavefront of 0.005 waves for pump beam of 817 nm). (B) 0.7 field (Strehl ratio of 0.993 and RMS wavefront of 0.014 waves for pump beam of 817 nm). (C) 1.0 field (Strehl ratio of 0.995 and RMS wavefront of 0.012 waves for pump beam of 817 nm). Red and blue marks denote Stokes and pump beam, respectively.

Stokes beam of 1064 nm. Therefore, it can be also said that ALM has perfectly diffraction-limited performance without chromatic aberrations considering the criterions of the Airy disk.

We have completed designs for both PLM and ALM. It's time to combine these modules to complete the whole system, namely probe-type microscope objective (PMO). After combining these modules, we have optimized again the whole system to eliminate some coupling disparities between PLM and ALM. As a result, we present the whole diagram of PMO in Fig. 13. For this PMO, spot diagrams are also presented in Fig. 14. Conclusively, it can be said that the final PMO has nearly diffraction-limited performance without chromatic aberrations for pump beam of 817 nm and Stokes beam of 1064 nm.

## V. CONCLUSION

For coherent anti-Stokes Raman scattering (CARS) microendoscopy for insertion into internal organs through a surgical keyhole with minimal invasiveness, we have designed a long slender probe-type objective, namely probe-type microscope objective (PMO) instead of a stack of GRIN rod lenses. The structure of PMO had to be composed of probe-type lens module (PLM) and adaptor lens module (ALM). For the design of PLM, the core issue was to design a long slender objective, which is controlled by two key factors: intermediate image height and NA at the sample side. And for the design of ALM, the core issue was to couple between the scanning unit and PLM, which is controlled by five design parameters: $f_a$, D, $\theta$, $\eta$, and NAO (Fig. 6). After completing designs for both PLM and ALM, the whole system, namely PMO, was optimized again to eliminate some coupling disparities between PLM and ALM. In conclusion, the final PMO has shown nearly diffraction-limited performance without chromatic aberrations for pump beam of 817 nm and Stokes beam of 1064 nm.

## ACKNOWLEDGMENT

This work has been supported by 2010 Hannam University Research Grant.

## REFERENCES

1. S. J. Jang, J. H. Kang, K. I. Kim, T. S. Lee, Y. J. Lee, K. C. Lee, K. S. Woo, W. S. Chung, H. C. Kwon, C. J. Ryu, T. H. Choi, C. W. Choi, S. M. Lim, and G. J. Cheon, "Application of bioluminescence imaging to therapeutic intervention of herpes simplex virus type I - thymidine kinase/ganciclovir in glioma," Cancer Letters **297**, 84-90 (2010).
2. Y. Waerzeggers, P. Monfared, T. Viel, A. Winkeler, and A. H. Jacobs, "Mouse models in neurological disorders: applications of non-invasive imaging," Biochimica et Biophysica Acta–Molecular Basis of Disease **1802**, 819-839 (2010).
3. B. W. Pogue, K. S. Samkoe, S. L. Gibbs-Strauss, and S. C. Davis, "Fluorescent molecular imaging and dosimetry tools in photodynamic therapy," Methods in Molecular Biology **635**, 207-222 (2010).
4. N. Olivier, M. A. Luengo-Oroz, L. Duloquin, E. Faure, T. Savy, I. Veilleux, X. Solinas, D. Débarre, P. Bourgine, A. Santos, N. Peyriéras, and E. Beaurepaire, "Cell lineage reconstruction of early zebrafish embryos using label-free nonlinear microscopy," Science **329**, 967-971 (2010).
5. S. J. Wallace, J. L. Morrison, K. J. Botting, and T. W. Kee, "Second-harmonic generation and two-photon-excited autofluorescence microscopy of cardiomyocytes: quantification of cell volume and myosin filaments," Journal of Biomedical Optics **13**, 064018 (2008).
6. C. Fiorini-Debuisschert, I. Berline, G. Metgé, F. Charra, M. Mihaly, C. Allain, G. Bordeau, and M. P. Teulade-Fichou, "Two-photon microscopy: from the optimisation of fluorescent DNA labels to local probe scanning second harmonic generation microscopy," Nonlinear Optics Quantum Optics

**38**, 271-280 (2009).
7. D. Aït-Belkacem, A. Gasecka, F. Munhoz, S. Brustlein, and S. Brasselet, "Influence of birefringence on polarization resolved nonlinear microscopy and collagen SHG structural imaging," Opt. Express **18**, 14467-14473 (2010).
8. Y. Sartenaer, L. Dreesen, C. Humbert, C. Volcke, G. Tourillon, P. Louette, P. A. Thiry, and A. Peremans, "Adsorption properties of decyl thiocyanate and decanethiol on platinum substrates studied by sum-frequency generation spectroscopy," Surface Science **601**, 1259-1264 (2007).
9. Y. S. Yoo, D. H. Lee, and H. Cho, "Differential two-signal picosecond-pulse coherent anti-Stokes Raman scattering imaging microscopy by using a dual-mode optical parametric oscillator," Opt. Lett. **32**, 3254-3256 (2007).
10. F. Lu, W. Zheng, and Z. Huang, "Coherent anti-Stokes Raman scattering microscopy using tightly focused radially polarized light," Opt. Lett. **34**, 1870-1872 (2009).
11. K. M. Hajek, B. Littleton, D. Turk, T. J. McIntyre, and H. Rubinsztein-Dunlop, "A method for achieving super-resolved widefield CARS microscopy," Opt. Express **18**, 19263-19272 (2010).
12. C. L. Evans, E. O. Potma, M. Puoris'haag, D. Côté, C. P. Lin, and X. S. Xie, "Chemical imaging of tissue in vivo with video-rate coherent anti-Strokes Raman scattering microscopy," Proceedings of the National Academy of Sciences of the United States of America **102**, 16807-16812 (2005).
13. R. S. Lim, A. Kratzer, N. P. Barry, S. Miyazaki-Anzai, M. Miyazaki, W. W. Mantulin, M. Levi, E. O. Potma, and B. J. Tromberg, "Multimodal CARS microscopy determination of the impact of diet on macrophage infiltration and lipid accumulation on plaque formation in ApoE-deficient mice," Journal of Lipid Research **51**, 1729-1737 (2010).
14. W. Göbel, J. N. D. Kerr, A. Nimmerjahn, and F. Helmchen, "Miniaturized two-photon microscope based on a flexible coherent fiber bundle and a gradient-index lens objective," Opt. Lett. **29**, 2521-2523 (2004).
15. M. J. Levene, D. A. Dombeck, K. A. Kasischke, R. P. Molloy, and W. W. Webb, "In vivo multiphoton microscopy of deep brain tissue," Journal of Neurophysiology **91**, 1908-1912 (2004).
16. J. C. Jung, A. D. Mehta, E. Aksay, R. Stepnoski, and M. J. Schnitzer, "In vivo mammalian brain imaging using one- and two-photon fluorescence microendoscopy," Journal of Neurophysiology **92**, 3121-3133 (2004).
17. P. Kim, M. Puoris'haag, D. Côté, C. P. Lin, and S. H. Yun, "In vivo confocal and multiphoton microendoscopy," Journal of Biomedical Optics **13**, 010501 (2008).
18. B. A. Flusberg, E. D. Cocker, W. Piyawattanametha, J. C. Jung, E. L. M. Cheung, and M. J. Schnitzer, "Fiber-optic fluorescence imaging," Nature Methods **2**, 941-950 (2005).
19. H. Wang, T. B. Huff, Y. Fu, K. Y. Jia, and J. X. Cheng, "Increasing the imaging depth of coherent anti-Stokes Raman scattering microscopy with a miniature microscope objective," Opt. Lett. **32**, 2212-2214 (2007).
20. R. L. Harzic, I. Riemann, M. Weinigel, K. König, and B. Messerschmidt, "Rigid and high-numerical-aperture two-photon fluorescence endoscope," Appl. Opt. **48**, 3396-3400 (2009).
21. C. S. Rim, "Design of an endoscope objective lens with a high numerical aperture and a minimally-invasive outer diameter," J. Korean Phys. Soc. **51**, 52-64 (2007).
22. X. Chen and N. George, "Resolution analysis of a gradient-index rod and a gradient-index lens array," Appl. Opt. **47**, 6190-6201 (2008).
23. J. X. Cheng, A. Volkmer, L. D. Book, and X. S. Xie, "Epi-detected coherent anti-Stokes Raman scattering (E-CARS) microscope with high spectral resolution and high sensitivity," Journal of Physical Chemistry B **105**, 1277-1280 (2001).
24. M. D. Duncan, J. Reintjes, and T. J. Manuccia, "Scanning coherent anti-Stokes Raman microscope," Opt. Lett. **7**, 350-352 (1982).
25. A. Zumbusch, G. R. Holtom, and X. S. Xie, "Three-dimensional vibrational imaging by coherent anti-Stokes Raman scattering," Phys. Rev. Lett. **82**, 4142-4145 (1999).
26. H. Alencar, U. Mahmood, Y. Kawano, T. Hirata, and R. Weissleder, "Novel multiwavelength microscopic scanner for mouse imaging," Neoplasia **7**, 977-983 (2005).
27. J. X. Cheng, "Coherent anti-Stokes Raman scattering microscopy," Applied Spectroscopy **61**, 197A-208A (2007).
28. Optical Research Associates, Inc., "CODE V version 10.0," http://www.opticalres.com.
29. W. J. Smith, *Modern Optical Engineering* (MacGraw-Hill, NY, USA, 2001), Chapter 6.
30. J.-U. Lee and S.-M. Yu, "Analytic design procedure of three-mirror telescope corrected for spherical aberration, coma, astigmatism, and Petzval field curvature," J. Opt. Soc. Korea **13**, 184-192 (2009).
31. Gyeong-Il Kweon, "Panoramic image composed of multiple rectilinear images generated from a single fisheye image," J. Opt. Soc. Korea **14**, 109-120 (2010).